Design of integral terminal sliding mode controller for the hybrid AC/DC microgrids involving renewables and energy storage systems

Hammad Armghan[a], Ming Yang[a],[*], Ammar Armghan[c], Naghmash Ali[a], M.Q. Wang[a], Iftikhar Ahmad[b]

[a] *School of Electrical Engineering, Shandong University, Jinan 250061, China*
[b] *Department of Electrical Engineering, National University of Sciences and Technology (NUST), Islamabad, Pakistan*
[c] *Department of Electrical Engineering, Jouf University, Sakaka, Saudi Arabia*

ABSTRACT

Traditional power generation is in the midst of a major transformation, and renewable based microgrids are playing a key role in this energy structure transition. This paper investigates the design of a centralized nonlinear controller based on the integral terminal and fast integral terminal sliding mode control for hybrid AC/DC microgrid involving renewable distributed generator as a primary source, fuel cell (FC) as a secondary source, and battery-ultracapacitor as hybrid energy storage system (HESS). At first, the detailed mathematical model of the hybrid AC/DC microgrid is established. Then, the controller is designed with the main objective to ensure the constant DC and AC bus voltage during islanding and grid-connected mode. During grid-connected mode, the controller is capable of providing frequency support to the utility grid. After that, the asymptotic stability of the hybrid AC/DC microgrid is proved using Lyapunov stability criteria. Then, the performance and robustness of the proposed control approach are tested by simulating it on MATLAB/Simulink, and the results are compared with sliding mode controller and Lyapunov redesign. Finally, real-time hardware in the loop tests are conducted to validate the effectiveness of the proposed framework.

1. Introduction

The emergence of renewable energy sources such as wind energy and PV energy is playing an essential role in the expansion of power generation [1]. Hence, hybrid AC/DC microgrids with renewables as distributed generation (DG) are witnessing rapid growth and capturing the interest of many researchers [2,3]. A typical hybrid AC/DC microgrid usually consists of DC subgrid and AC subgrid, which are interlinked through bidirectional power converters. The AC/DC microgrid combines the advantage of both AC microgrid and DC microgrid [1]. Specifically, it can support both AC and DC loads without any unnecessary AC-to-DC and DC-to-AC conversions. Consequently, it reduces the energy losses by minimizing the multiconversion processes [4]. The wind power capacity reached 597GW by the end of 2018 and accounts for 20.3% of the world's market share [5]. However, due to the unpredictable nature of wind energy, it cannot provide steady power. Hence, the integration of reliable energy sources with renewable energy sources is essential for the stable operation of the microgrids [6].

The proton exchange membrane (PEM) fuel cell (FC) is an electrochemical energy source that can provide constant energy but has the limitation of slow dynamic response to power transients [6,7]. The combination of wind and FC is an effective way to provide steady power, but an instant change in load demand can have a drastic effect on the performance of the microgrid [8]. To avoid such issues, hybrid energy storage systems (HESSs), which are the combination of battery banks and ultracapacitors (UCs) are introduced [9].

HESSs can absorb and supply the steady and transient power to ensure the stable operation of the microgrid. The combination of battery and UC is studied in [10,11]. It can be seen that the introduction of high power density components in energy storage systems (ESSs) such as UCs to provide support for transient load demand can improve the lifetime of the battery by operating it within its rated values. Thus, the wind energy system as a main source and FC as a secondary source with the battery-UC combination as HESS can be a promising solution to operate the AC/DC microgrid. However, the intermittency in wind energy and variation in AC/DC loads could result in the fluctuation of DC link bus voltage and unstable operation of AC/DC microgrid [12].

* Corresponding author.
E-mail addresses: 14mseeharmghan@seecs.edu.pk (H. Armghan), myang@sdu.edu.cn (M. Yang), aarmghan@ju.edu.sa (A. Armghan), 14mseenmr@seecs.edu.pk (N. Ali), wang0367@sdu.edu.cn (M.Q. Wang), iftikhar.rana@seecs.edu.pk (I. Ahmad).

Hence, the effective control strategy to regulate the DC bus voltage and to ensure the power balance is important for the normal operation of AC/DC microgrid. Furthermore, stable voltage and frequency of the AC subgrid are one of the critical control challenges as well.

Different control strategies for the DC microgrids have been suggested with the main goal to regulate the DC bus voltage [13–18]. Since the control and optimization of a hybrid AC/DC microgrid involve complex operation because of the coexistence of AC and DC microgrids [19]. Hence, these methods cannot be applied directly to AC/DC microgrids. Different schemes for the control of AC/DC microgrids have been studied in the literature. A hybrid AC/DC microgrid that can operate in grid-connected and islanding mode is proposed in [20]. In islanding mode, an inverter is used for the regulation of voltage and frequency in AC subgrid, and power converters regulate the common DC bus voltage. In grid connected mode, the AC side acts as an infinite bus. Hence, the only concern is the stabilization of the DC common bus, which is ensured by the inverter. Few other control techniques have also been applied to a similar AC/DC microgrid configuration. However, the intermittency of renewable energy sources is not considered in these studies [21,22].

In [23], flatness based fuzzy logic controller is proposed for renewable based hybrid microgrid, but the operation is only limited to the islanding mode, and the energy management system generates the reference signal for FC without considering the effect of over and under-utilization of H_2. A distributed control technique for bidirectional converters interlinking AC and DC subgrids is presented in [24], but the dynamics of converters are not considered in this study. A droop-based controller is implemented in [25–27], to ensure power the balance in AC/DC microgrid. On the contrary, the method has its limitations when multiple energy sources are connected together and offers poor voltage regulation. Several other linear control techniques for the islanding and grid-connected control of hybrid AC/DC microgrid have been reported in [28,19,12,29], but the dynamics of renewable energy sources and power converters are not studied. Furthermore, these linear controllers show sensitivity to the nonlinearities presented in the wind, FC and ESSs.

Few nonlinear control techniques have also been proposed for the hybrid AC/DC microgrid [30–32]. Decentralized sliding mode control is proposed in [33] to improve the stability and power management of hybrid AC/DC microgrid. However, the paper discusses the performance of microgrid in islanding mode only. Furthermore, two controllers were designed to ensure a stable operation, which results in complexity. Output feedback linearization and backstepping control for hybrid AC/DC microgrid have been reported in [34,35]. However, the considered microgrid in these studies consists of fewer components and doesn't involve multiple DGs. In [36], Lyapunov based control is designed for the renewable based hybrid AC/DC Microgrid providing ancillary services to the AC subgrid in grid-connected mode. Ancillary services involve providing frequency support, voltage control, reactive power compensation, and so on to ensure the stability of the power system [37].

The modeling and control for hybrid AC/DC microgrids involving different DGs, ESSs and loads have always been challenging. The intermittent nature of renewable can have drastic effect on the grid stability [18]. On the other hand, constant power loads (CPLs) which are connected to the DC side of the grid are known to degrade the overall performance of the system as well [36]. Furthermore, the switching between islanding and grid-connected mode can result in DC and AC bus voltage fluctuation [38]. Hence, a more advance control action is required to ensure the stable operation of microgrid under varying generation, operating condition and load demand. Different from current literature, a comprehensive global mathematical model for the hybrid AC/DC microgrid is formulated and a centralized integral terminal sliding mode based more robust and efficient control action is developed for different components connected to the hybrid AC/DC microgrid. By further advancing the application of proposed

framework, the possibility of providing ancillary service to the utility grid is also studied. It should be noted that unlike conventional control, the proposed framework does not require an outer voltage loop and an inner current loop, which further reduces the complication involved in the process. The asymptotic stability of the microgrid is ensured using Lyapunov stability criteria. The main contributions of the proposed method are as follow: (1) Introduction of the centralized nonlinear robust controller based on integral terminal and fast integral terminal sliding mode for wind-FC-battery-UC hybrid AC/DC microgrid that can operate in both islanding and grid-connected mode, (2) The same controller will perform maximum power point tracking (MPPT), common DC and AC bus voltage regulation and current tracking, regardless of the mode of operation, (3) During grid-connected mode, the proposed controller provides the frequency support to the AC side while ensuring the stable operation of the DC side, (4) The performance of the proposed controller is validated through MATLAB/Simulink software environment and real-time controller hardware in the loop analysis.

The rest of the paper is outlined as follows: In Section 2, the dynamic modeling of the hybrid AC/DC microgrid is introduced. Section 3 depicts the proposed integral terminal sliding mode control for the hybrid AC/DC microgrid. Section 4 shows the simulation and hardware results and comparison with sliding mode control and Lyapunov redesign. Section 5 concludes the article.

2. The dynamical modeling of microgrid components

Fig. 1 presents the configuration of the considered renewable based hybrid AC/DC microgrid. It consists of 6 nodes, 5 DC lines and AC and DC loads. Each node represents the underlying dynamical subsystem. The node 1 contains the wind energy system, in which the wind turbine is connected to the DC common bus through permanent magnet synchronous generator (PMSG) and DC-DC boost converter. The FC is connected to the DC common bus via DC-DC boost converter and represents the node 2. Both the energy storage sources (battery, UC) are interfaced directly to the DC common bus via bidirectional DC-DC converters and constitute our node 3 and 4. These storage devices will play a key role in the stabilization of AC/DC microgrid. Node 5 consists of CPLs which are connected to the DC side of the grid. Finally, node 6 contains interlinking converter and linear AC loads. The detailed configuration of the considered system is presented in Table 3. When S_G is off, the system will operate in islanding mode and will only provide power to local AC and DC loads. When S_G is on, the system will operate in grid-connected mode and will provide frequency support to the utility gird. The mathematical modeling of the microgrid components is essential for the development of control law. These models are presented in detail as follow.

2.1. Modeling of wind turbine system

Fig. 2 shows the configuration of the wind energy system. It includes a wind turbine, an uncontrolled rectifier, PMSG, and a DC-DC power converter. The wind energy system is connected to the DC common bus through DC-DC boost converter and can be operated at MPPT and OFF-MPPT mode as instructed by the high-level controller.

The mechanical power produced by the wind turbine can be presented as [39]:

$$P_m = 0.5\rho\pi r^2 v_m^3 C_p(\lambda, \beta), \tag{1}$$

where r is the turbine radius, v_m is the wind speed, and ρ (kg/m^3) is air density. Whereas C_p is the turbine power coefficient and can be written as the function of tip speed ratio (λ) and the blade pitch angle (β). Usually, the value of C_p lies between 0.4 and 0.45. λ can be written as:

$$\lambda = \frac{\omega_m r}{v_m}, \tag{2}$$

where ω_m (rad/s) is the angular velocity of the rotor. By substituting the
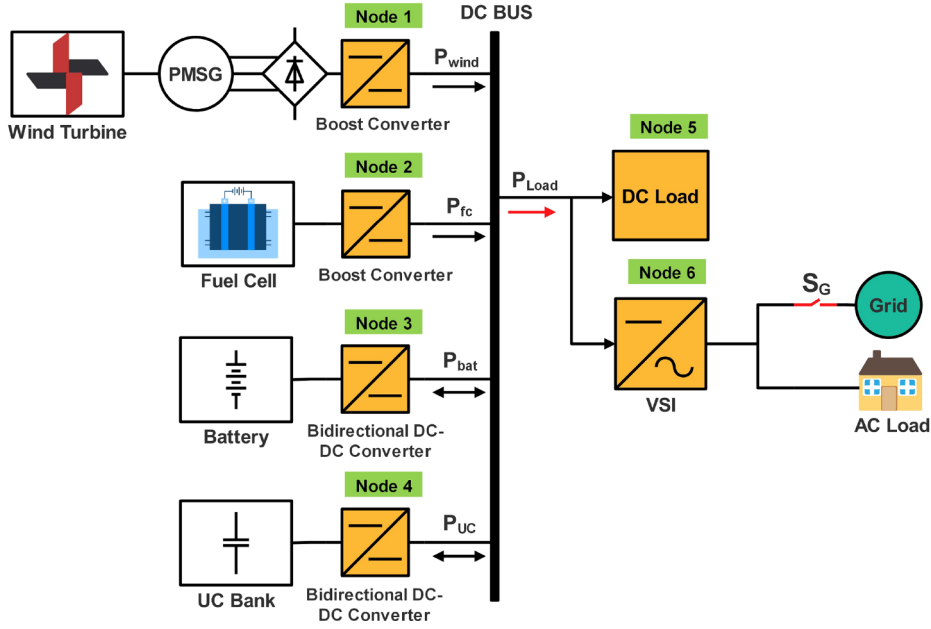
Fig. 1. The considered hybrid AC/DC microgrid.

value of v_m from (2) into (1), we get:

$$P_m = \frac{1}{2}\rho\pi r^5 \frac{\omega_m^3}{\lambda^3} C_p. \tag{3}$$

For MPPT, this paper utilizes the optimal torque control (OTC) method. This method has the advantage of being simple and accurate [39]. The OTC technique works by varying the torque of PMSG at given wind speed to a maximum reference torque of the wind turbine. By assuming that the rotor has an optimum tip-speed ratio and maximum power coefficient, we can replace λ and C_p with λ_{op} and C_{pmax}. Now, (3) can be rewritten as:

$$P_{m-op} = \frac{1}{2}\rho\pi r^5 \frac{C_{pmax}}{\lambda_{op}^3}\omega_m^3 = K_{p-op}\omega_m^3. \tag{4}$$

Since $P_{m-op} = \omega_m T_{m-op}$, we can rewrite (4) as:

$$T_{m-op} = \frac{1}{2}\rho\pi r^5 \frac{C_{pmax}}{\lambda_{op}^3}\omega_m^2 = K_{p-op}\omega_m^2. \tag{5}$$

Using (5), reference torque T_{m-op} can be calculated and from that, we can determine the value of reference current I_{wref} using the equation mentioned below:

$$I_{wref} = \frac{T_{m-op} \times \omega_m}{V_w}, \tag{6}$$

where V_w is output DC voltages from the uncontrolled rectifier. DC-DC boost converter controls the rotational speed of the PMSG by acting as an apparent load. It consists of an input inductor L_w, diode D, output filter capacitor C_{dc} and IGBT switch S_1. The mathematical model of the wind power converter can be presented with the following set of differential equations:

$$\frac{di_w}{dt} = \frac{V_w}{L_w} - \frac{R_w}{L_w}i_w - (1-\mu_1)\frac{v_{dc}}{L_w}, \tag{7}$$

$$\frac{dv_{dc}}{dt} = (1-\mu_1)\frac{i_w}{C_{dc}} - \frac{I_w'}{C_{dc}}, \tag{8}$$

where i_w, v_{dc}, and μ_1 are the wind current, output voltage, and control signal, respectively.
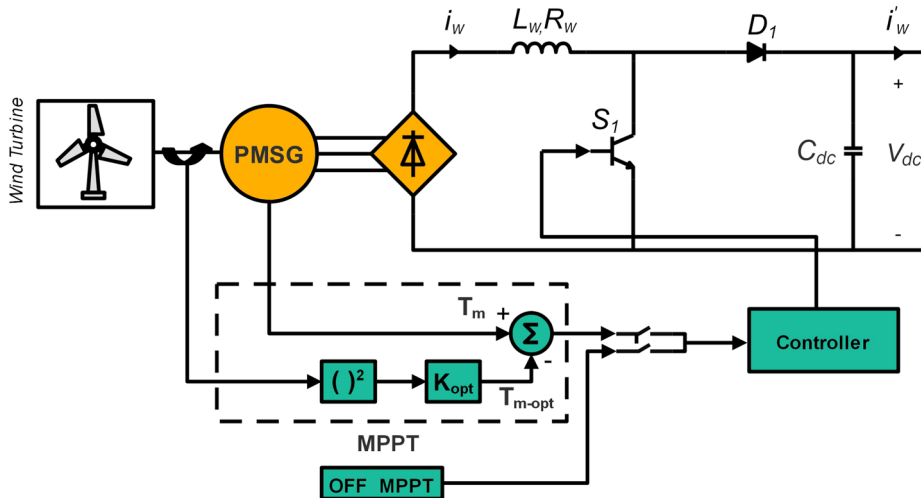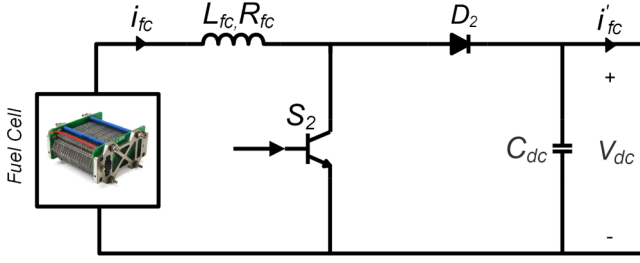

Fig. 2. Wind system configuration.

Fig. 3. Fuel cell configuration.

2.2. Modeling of fuel cell system

FC can provide reliable and clean power. It is connected to the DC common bus through DC-DC boost converter operating in current control mode as shown in Fig. 3. The voltage (V_{fcell}) of the FC can be expressed as:

$$V_{fcell} = E + \eta_a + \eta_{ohm}, \tag{9}$$

where E is the Nernst instantaneous voltage, η_a and η_{ohm} are the activation overvoltage and ohmic overvoltage, respectively. Hydrogen utilization factor (U_h) is an important parameter for the stable operation of FC, and it can be written as:

$$U_h = q_{h2}^{rea}/q_{h2}^{in}, \tag{10}$$

where q_{h2}^{rea} is the amount of H_2 reacted inside the tank, and q_{h2}^{in} is the amount of H_2 injected into the tank. It should be remembered that the value of U_h above 0.9 corresponds to the over-utilization of hydrogen, which results in the fuel starvation phenomenon, and could have a drastic effect on the life-span of FC. Contrary, if the value of U_h is below 0.8, it indicates the under-utilization of hydrogen, leading to the unstable output voltage, and poor power efficiency. For the optimal utilization of H_2, the FC current (I_{fc}) is limited by following equation:

$$\frac{0.8q_{h2}^{in}}{2K_c} \leqslant I_{fc} \leqslant \frac{0.9q_{h2}^{in}}{2K_c}, \tag{11}$$

where K_c is the modeling constant. The current reference (I_{fcref}) for the FC is obtained from the high-level controller. The mathematical model of the boost converter can be described using the following differential equations:

$$\frac{di_{fc}}{dt} = \frac{V_{fc}}{L_{fc}} - \frac{R_{fc}}{L_{fc}}i_{fc} - (1 - \mu_2)\frac{v_{dc}}{L_{fc}}, \tag{12}$$

$$\frac{dv_{dc}}{dt} = (1 - \mu_2)\frac{i_{fc}}{C_{dc}} - \frac{I'_{fc}}{C_{dc}}, \tag{13}$$

where i_{fc}, v_{dc}, and μ_2 are the FC current, output voltage, and control signal, respectively.

2.3. Modeling of hybrid energy storage system

Due to the unpredictable nature of wind energy, and the limitation of FC power, HESS are used to ensure the power balance. The HESS considered in this study consists of a battery and UC. Both the energy storage sources are connected to the DC common bus through bidirectional DC-DC buck-boost converters as shown in Fig. 4a and b.
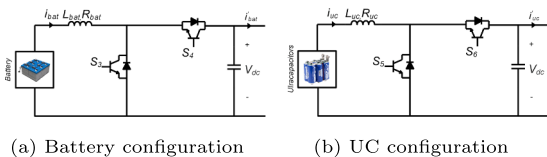

(a) Battery configuration   (b) UC configuration

Fig. 4.

The mathematical model of the battery's buck boost converter is introduced by the following set of equations:

$$\frac{di_{bat}}{dt} = \frac{V_{bat}}{L_{bat}} - \frac{R_{bat}}{L_{bat}}i_{bat} - (\mu_{34})\frac{v_{dc}}{L_{bat}}, \tag{14}$$

$$\frac{dv_{dc}}{dt} = (\mu_{34})\frac{i_{bat}}{C_{dc}} - \frac{I'_{bat}}{C_{dc}}, \tag{15}$$

where i_{bat}, v_{dc}, and μ_{34} are the battery current, output voltage, and control signal, respectively. The detailed mathematical modeling of the HESS is already discussed in [18]. Similarly, the mathematical model of the UC's buck boost converter can be expressed as:

$$\frac{di_{uc}}{dt} = \frac{V_{uc}}{L_{uc}} - \frac{R_{uc}}{L_{uc}}i_{uc} - (\mu_{56})\frac{v_{dc}}{L_{uc}}, \tag{16}$$

$$\frac{dv_{dc}}{dt} = (\mu_{56})\frac{i_{uc}}{C_{dc}} - \frac{I'_{uc}}{C_{dc}}, \tag{17}$$

where i_{uc}, v_{dc}, and μ_{56} are the UC current, output voltage, and control signal, respectively.

2.4. Modeling of AC subgrid

Fig. 5 shows the configuration of the AC side. The three-phase voltage source inverter (VSI) is utilized to supply power to AC loads and utility grid. The voltages and currents of the VSI are as follows; V_d, V_q, I_d, and I_q are the dq axis output currents and voltages; I_{ld}, and I_{lq} are the dq axis currents of the load inductor; V_{gd}, V_{gq}, I_{gd}, and I_{gq} are the dq axis utility grid currents and voltages. Both AC loads and utility grid are operating at same frequency and voltages. The mathematical model of the VSI, which is obtained using Park and Clark's dq transformation can be expressed as [38]:

$$\frac{dV_d}{dt} = -\frac{V_d}{RC_f} + w_oV_q + \frac{I_d}{C_f} - \frac{I_{ld}}{C_f} - \frac{I_{gd}}{C_f}, \tag{18}$$

$$\frac{dV_q}{dt} = -\frac{V_q}{RC_f} - w_oV_d + \frac{I_q}{C_f} - \frac{I_{lq}}{C_f} - \frac{I_{gq}}{C_f}, \tag{19}$$

$$\frac{dI_d}{dt} = -\frac{V_d}{L_f} - \frac{R_fI_d}{L_f} + w_oI_q + \frac{U_dV_{dc}}{L_f}, \tag{20}$$

$$\frac{dI_q}{dt} = -\frac{V_q}{L_f} - \frac{R_fI_q}{L_f} - w_oI_q + \frac{U_qV_{dc}}{L_f}, \tag{21}$$

$$\frac{dI_{ld}}{dt} = \frac{V_d}{L_l} - \frac{R_lI_{ld}}{L_l} + w_oI_{lq}, \tag{22}$$

$$\frac{dI_{lq}}{dt} = \frac{V_q}{L_l} - \frac{R_lI_{lq}}{L_l} - w_oI_{ld}, \tag{23}$$

$$\frac{dI_{gd}}{dt} = \frac{V_d}{L_g} - \frac{R_gI_{gd}}{L_g} + w_oI_{gq} - \frac{V_{gd}}{L_g}, \tag{24}$$

$$\frac{dI_{gq}}{dt} = \frac{V_q}{L_g} - \frac{R_gI_{gq}}{L_g} - w_oI_{gd} - \frac{V_{gq}}{L_g}, \tag{25}$$

$$\frac{dw_o}{dt} = \alpha\left[P_m + \frac{3}{2}(V_dI_d - V_qI_q)\right], \tag{26}$$

where R_f, C_f, and L_f are the variables expressing the equivalent resistance, the capacitance, and the inductance of the LC filter, respectively. L_g, and are the coupling inductance and its equivalent resistance, respectively. Whereas L_l, and R_l are the load inductance and its equivalent resistance, respectively. w_o is the angular frequency of the VSI's output voltage. where α is based on the inertia of AC generators, and P_m is the mechanical power.
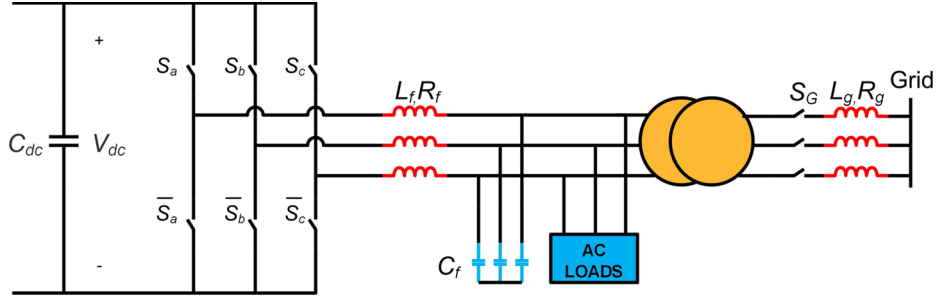
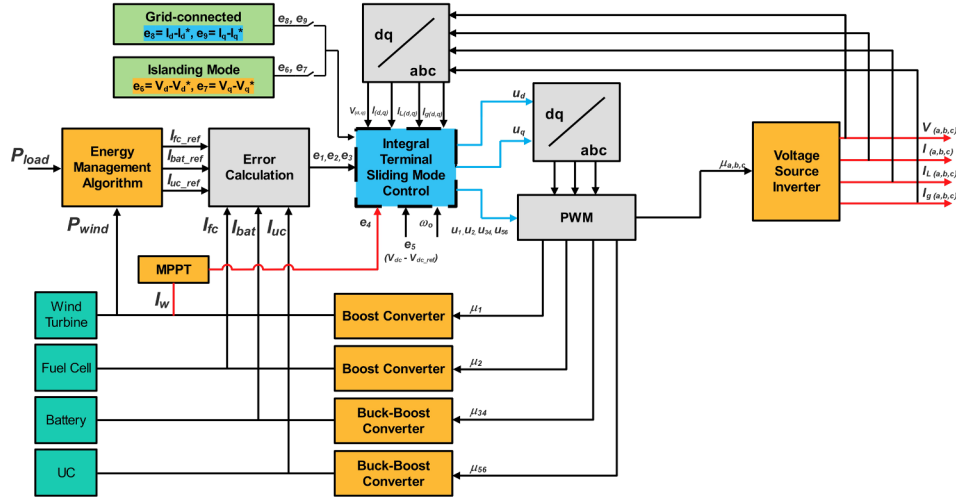**Fig. 5.** AC subgrid configuration.

Fig. 6. General structure of the controlled system.

2.5. Hybrid AC/DC microgrid global modeling

The global model of hybrid AC/DC microgrid comprises of renewable energy source, FC, storage units (battery and UC), DC and AC loads, and AC subgrid can be obtained using the models suggested in Sections 2.1, 2.2, 2.3, and 2.4 as follows:

$$\frac{dx_1}{dt} = \frac{V_w}{L_w} - \frac{R_w}{L_w}x_1 - (1 - \mu_1)\frac{x_5}{L_w}, \tag{27}$$

$$\frac{dx_2}{dt} = \frac{V_{fc}}{L_{fc}} - \frac{R_{fc}}{L_{fc}}x_2 - (1 - \mu_2)\frac{x_5}{L_{fc}}, \tag{28}$$

$$\frac{dx_3}{dt} = \frac{V_{bat}}{L_{bat}} - \frac{R_{bat}}{L_{bat}}x_3 - (\mu_{34})\frac{x_5}{L_{bat}}, \tag{29}$$

$$\frac{dx_4}{dt} = \frac{V_{uc}}{L_{uc}} - \frac{R_{uc}}{L_{uc}}x_4 - (\mu_{56})\frac{x_5}{L_{uc}}, \tag{30}$$

$$\frac{dx_5}{dt} = (1 - \mu_1)\frac{x_1}{C_{dc}} + (1 - \mu_2)\frac{x_2}{C_{dc}} + (\mu_{34})\frac{x_3}{C_{dc}} + (\mu_{56})\frac{x_4}{C_{dc}} - \frac{I_{dc}}{C_{dc}} - \frac{3}{2C_{dc}x_5}[x_6x_8 + x_7x_9], \tag{31}$$

$$\frac{dx_6}{dt} = -\frac{x_6}{RC_f} + x_{14}x_7 + \frac{x_8}{C_f} - \frac{x_{10}}{C_f} - \frac{x_{12}}{C_f}, \tag{32}$$

$$\frac{dx_7}{dt} = -\frac{x_7}{RC_f} - x_{14}x_6 + \frac{x_9}{C_f} - \frac{x_{11}}{C_f} - \frac{x_{13}}{C_f}, \tag{33}$$

$$\frac{dx_8}{dt} = -\frac{x_6}{L_f} - \frac{R_f x_8}{L_f} + x_{14}x_9 + \frac{U_d x_5}{L_f}, \tag{34}$$

$$\frac{dx_9}{dt} = -\frac{x_7}{L_f} - \frac{R_f x_9}{L_f} - x_{14}x_8 + \frac{U_q x_5}{L_f}, \tag{35}$$

$$\frac{dx_{10}}{dt} = \frac{x_6}{L_l} - \frac{R_l x_{10}}{L_l} + x_{14}x_{11}, \tag{36}$$

$$\frac{dx_{11}}{dt} = \frac{x_7}{L_l} - \frac{R_l x_{11}}{L_l} - x_{14}x_{10}, \tag{37}$$

$$\frac{dx_{12}}{dt} = \frac{x_6}{L_g} - \frac{R_g x_{12}}{L_g} + x_{14}x_{13} - \frac{W_1}{L_g}, \tag{38}$$

$$\frac{dx_{13}}{dt} = \frac{x_7}{L_g} - \frac{R_g x_{13}}{L_g} - x_{14}x_{12} - \frac{W_2}{L_g}, \tag{39}$$

$$\frac{dx_{14}}{dt} = \alpha\left[P_m - \frac{3}{2}(x_6x_8 + x_7x_9)\right], \tag{40}$$

where x_1, x_2, x_3, and x_4 are the currents of the inductors L_w, L_{fc}, L_{bat}, and L_{uc}; x_5 is the voltages of capacitor C_{dc}; x_6, x_7, x_8, and x_9 are the dq axis voltages and currents; x_{10}, and x_{11} are the currents of the AC load; x_{12}, x_{13}, W_1 and W_2 are the currents and voltages of the utility grid, while x_{14} is the angular frequency. The controller design is discussed in the next section to regulate the common DC bus and AC bus voltages during islanding and gird-connected mode.

3. Proposed integral terminal sliding mode based control strategy

Fig. 6 shows the general structure of the implemented control scheme. A centralized integral terminal sliding mode based nonlinear control strategy is presented in this work with the main aim to ensure the stable operation of the microgrid. Furthermore, the objectives of the

proposed control method can be summarized as:

1. Regulation of the common DC bus voltage at the DC subgrid.
2. Guaranteeing the AC and DC loads services.
3. Smooth transition between islanding and grid-connected operation of the microgrid.
4. Frequency support to the utility grid during the grid-connected mode.
5. Asymptotical stability of the whole microgrid.

For the stable operation of the microgrid, the tracking error trajectories can be expressed as:

$$
\begin{Bmatrix} e_1 \\ e_2 \\ e_3 \\ e_4 \\ e_5 \\ e_6 \\ e_7 \\ e_8 \\ e_9 \end{Bmatrix} = \begin{Bmatrix} x_1 - x_1^* \\ x_2 - x_2^* \\ x_3 - x_3^* \\ x_4 - x_4^* \\ x_5 - x_5^* \\ x_6 - x_6^* \\ x_7 - x_7^* \\ x_8 - x_8^* \\ x_9 - x_9^* \end{Bmatrix},
\tag{41}
$$

where x_1^*, x_2^*, x_3^*, and x_4^* are the reference current values for the wind system (MPPT), FC, battery, and UC. Whereas x_5^* is the desired common DC bus voltage. x_6^*, and x_7^* are the reference dq voltages for the VSI when the switch S_G is off and the system is operating in islanding mode. x_8^*, and x_9^* are the reference dq currents for the VSI when the switch S_G is on and the system is operating in grid-connected mode. It is worth noting that the reference values are generated by high-level controller based on the operating mode. Defining the integral terminal sliding mode surfaces:

$$
S_1 = e_1 + K_1 \left(\int_0^t e_1 dt \right)^{\lambda_1},
\tag{42}
$$

$$
S_2 = e_2 + K_2 \left(\int_0^t e_2 dt \right)^{\lambda_2},
\tag{43}
$$

$$
S_3 = e_3 + K_3 \left(\int_0^t e_3 dt \right)^{\lambda_3},
\tag{44}
$$

$$
S_4 = e_4 + K_4 \left(\int_0^t e_4 dt \right)^{\lambda_4},
\tag{45}
$$

$$
S_5 = e_5 + K_5 \left(\int_0^t e_5 dt \right)^{\lambda_5},
\tag{46}
$$

where $K_i > 0$ is the design parameter of the controller, and $1 < \lambda_i < 2$ is the positive number. Whereas $i = 1, 2, 3, 4, 5$. Integral actions are added to the sliding surfaces to improve the steady state response and robustness of the controller. Taking the derivative of the sliding surfaces yield:

$$
\dot{S}_1 = \dot{e}_1 + K_1 e_1 (\lambda_1) \left(\int_0^t e_1 dt \right)^{\lambda_1 - 1},
\tag{47}
$$

$$
\dot{S}_2 = \dot{e}_2 + K_2 e_2 (\lambda_2) \left(\int_0^t e_2 dt \right)^{\lambda_2 - 1},
\tag{48}
$$

$$
\dot{S}_3 = \dot{e}_3 + K_3 e_3 (\lambda_3) \left(\int_0^t e_3 dt \right)^{\lambda_3 - 1},
\tag{49}
$$

$$
\dot{S}_4 = \dot{e}_4 + K_4 e_4 (\lambda_4) \left(\int_0^t e_4 dt \right)^{\lambda_4 - 1},
\tag{50}
$$

$$
\dot{S}_5 = \dot{e}_5 + K_5 e_5 (\lambda_5) \left(\int_0^t e_5 dt \right)^{\lambda_5 - 1}.
\tag{51}
$$

Substituting the value of $\dot{e}_1$ in (47) gives:

$$
\dot{S}_1 = \frac{V_w}{L_w} - \frac{R_w}{L_w} x_1 - (1 - \mu_1) \frac{x_5}{L_w} - \dot{x}_1^* + K_1 e_1 (\lambda_1) \left(\int_0^t e_1 dt \right)^{\lambda_1 - 1}.
\tag{52}
$$

For Lyapunov stability, which requires $\dot{V} \leq 0$ and convergence of errors dynamics to zero, control laws must be selected for $\dot{S}_k$ to behave as follows:

$$
\dot{S}_k = -\rho_k sgn(S_k),
\tag{53}
$$

where $\rho_k > 0$ and $k = 1, 2, 3, 4, 5$. Whereas sgn represents the signum function and can be written as:

$$
sgn(x) = \begin{cases} \frac{x}{|x|} & x \neq 0 \\ 0 & x = 0 \end{cases}
\tag{54}
$$

By comparing (52), and (53), control law μ_1 can be obtained as follows:

$$
\mu_1 = \frac{L_w}{x_5} \left[-\rho_1 sgn(S_1) - \frac{V_w}{L_w} + \frac{R_w}{L_w} x_1 \right] + \frac{L_w}{x_5} [\dot{x}_1^* - K_1 e_1 (\lambda_1)(\int_0^t e_1 dt)^{\lambda_1 - 1}] + 1,
\tag{55}
$$

where μ_1 is the duty cycle signal generated for the converter connecting the wind energy system to the DC common bus, and is bounded by $0 < \mu_1 < 1$. Similarly, by substituting the values of $\dot{e}_2$, $\dot{e}_3$, and $\dot{e}_4$ in (48)–(50) will give us the following set of equations:

$$
\dot{S}_2 = \frac{V_{fc}}{L_{fc}} - \frac{R_{fc}}{L_{fc}} x_2 - (1 - \mu_2) \frac{x_5}{L_{fc}} - \dot{x}_2^* + K_2 e_2 (\lambda_2) \left(\int_0^t e_2 dt \right)^{\lambda_2 - 1},
\tag{56}
$$

$$
\dot{S}_3 = \frac{V_{bat}}{L_{bat}} - \frac{R_{bat}}{L_{bat}} x_3 - (\mu_{34}) \frac{x_5}{L_{bat}} - \dot{x}_3^* + K_3 e_3 (\lambda_3) \left(\int_0^t e_3 dt \right)^{\lambda_3 - 1},
\tag{57}
$$

$$
\dot{S}_4 = \frac{V_{uc}}{L_{uc}} - \frac{R_{uc}}{L_{uc}} x_4 - (\mu_{56}) \frac{x_5}{L_{uc}} - \dot{x}_4^* + K_4 e_4 (\lambda_4) \left(\int_0^t e_4 dt \right)^{\lambda_4 - 1}.
\tag{58}
$$

Using (56)–(58), and (53), following control laws are introduced to stabilize the dynamics existed in FC and HESS:

$$
\mu_2 = \frac{L_{fc}}{x_5} \left[\frac{R_{fc}}{L_{fc}} x_2 - \rho_2 sgn(S_2) - \frac{V_{fc}}{L_{fc}} \right] + \frac{L_{fc}}{x_5} [\dot{x}_2^* - K_2 e_2 (\lambda_2)(\int_0^t e_2 dt)^{\lambda_2 - 1}] + 1,
\tag{59}
$$

$$
\mu_{34} = \frac{L_{bat}}{x_5} \left[\rho_3 sgn(S_3) + \frac{V_{bat}}{L_{bat}} - \frac{R_{bat}}{L_{bat}} x_3 \right] + \frac{L_{bat}}{x_5} [-\dot{x}_3^* + K_3 e_3 (\lambda_3)(\int_0^t e_3 dt)^{\lambda_3 - 1}],
\tag{60}
$$

$$
\mu_{56} = \frac{L_{uc}}{x_5} \left[\rho_4 sgn(S_4) + \frac{V_{uc}}{L_{uc}} - \frac{R_{uc}}{L_{uc}} x_4 \right] + \frac{L_{uc}}{x_5} [-\dot{x}_4^* + K_4 e_4 (\lambda_4)(\int_0^t e_4 dt)^{\lambda_4 - 1}],
\tag{61}
$$

where μ_2 is the duty cycle signal for the converter connected to the FC system. Whereas μ_{34}, and μ_{56} are the duty cycle signal for the converters connected to the battery, and UC, respectively. It is worth mentioning that all the control signals are bounded between 0 and 1. The desired value x_5^* of the common DC bus voltage can be obtained by substituting the value of $\dot{e}_4$ in (51):

$$
\dot{S}_5 = (1 - \mu_1) \frac{x_1}{C_{dc}} + (1 - \mu_2) \frac{x_2}{C_{dc}} + (\mu_{34}) \frac{x_3}{C_{dc}} + (\mu_{56}) \frac{x_4}{C_{dc}} - \frac{I_{dc}}{C_{dc}} - \frac{3}{2 C_{dc} x_5} [x_6 x_8 + x_7 x_9] + K_5 e_5 (\lambda_5)(\int_0^t e_5 dt)^{\lambda_5 - 1} - \dot{x}_5^*,
\tag{62}
$$

By comparing (53), and (62), x_5^* can be calculated as follows:

$$
x_5^* = (1 - \mu_1) \frac{x_1}{C_{dc}} + (1 - \mu_2) \frac{x_2}{C_{dc}} + (\mu_{34}) \frac{x_3}{C_{dc}} + (\mu_{56}) \frac{x_4}{C_{dc}} - \frac{I_{dc}}{C_{dc}} - \frac{3}{2 C_{dc} x_5} [x_6 x_8 + x_7 x_9] + K_5 e_5 (\lambda_5)(\int_0^t e_5 dt)^{\lambda_5 - 1} + \rho_5 sgn(S_5).
\tag{63}
$$

Now, the next step is to find the control laws for the AC subgrid. During the islanding mode, the common DC bus voltage is regulated by HESS,

while the DC/AC inverter is utilized to regulate the AC voltages for the AC loads. With this goal, following reference trajectories x_6^*, and x_7^* are defined for the dynamics x_6, and x_7. The dynamics show that the relative degree of the system is 2. Hence, fast integral terminal sliding mode control is implemented to obtain the control laws. The nominal angular frequency during islanding mode is modeled as $x_{14} = 2\pi f_0$. Let us take the derivative of the first tracking error e_6 given in (53):

$$\dot{e}_6 = \dot{x}_6 - \dot{x}_6^*. \tag{64}$$

Putting the value of $\dot{x}_6$ from (32) in (64) gives:

$$\dot{e}_6 = -\frac{x_6}{RC_f} + x_{14}x_7 + \frac{x_8}{C_f} - \frac{x_{10}}{C_f} - \frac{x_{12}}{C_f} - \dot{x}_6^*. \tag{65}$$

The second tracking error is introduced for the fast convergence and can be expressed as:

$$z_7 = \dot{e}_6. \tag{66}$$

Taking the derivative of (66) and using (32), (33), (34), (36), (38), and (40), the equation can be rewritten as:

$$\dot{z}_7 = -\frac{x_6}{C_f L_f} - \frac{R_f x_8}{C_f L_f} + \frac{x_{14}x_9}{C_f} + \frac{U_d x_5}{C_f L_f} \\ - M_1 + M_2 + M_3 - M_4 - M_5 - \ddot{x}_6^*, \tag{67}$$

where, M_1, M_2, M_3, M_4 and M_5 are introduced to simply the calculations and can be expressed as:

$$M_1 = \frac{1}{RC_f}\left[-\frac{x_6}{RC_f} + x_{14}x_7 + \frac{x_8}{C_f} - \frac{x_{10}}{C_f} - \frac{x_{12}}{C_f}\right],$$
$$M_2 = x_7 \dot{x}_{14},$$
$$M_3 = x_{14}\left[-\frac{x_7}{RC_f} - x_{14}x_6 + \frac{x_9}{C_f} - \frac{x_{11}}{C_f} - \frac{x_{13}}{C_f}\right],$$
$$M_4 = \frac{1}{C_f}\left[\frac{x_7}{L_l} - \frac{R_l x_{11}}{L_l} - x_{14}x_{10}\right],$$
$$M_5 = \frac{1}{C_f}\left[\frac{x_6}{L_g} - \frac{R_g x_{12}}{L_g} + x_{14}x_{13} - \frac{W_1}{L_g}\right]. \tag{68}$$

Defining the fast integral terminal sliding mode surface:

$$S_6 = z_7 + c_6 e_6 + K_6\left(\int_0^t e_6 dt\right)^{\lambda_6}, \tag{69}$$

where $c_6 > 0$ and $K_6 > 0$ are the design parameters, and λ_6 is the positive number. Taking the derivative of S_6 yields:

$$\dot{S}_6 = \dot{z}_7 + c_6 \dot{e}_6 + K_6 e_6(\lambda_6)\left(\int_0^t e_6 dt\right)^{\lambda_6 - 1}. \tag{70}$$

By substituting the values of $\dot{e}_6$ and $\dot{z}_7$ in (70), the equation can be rewritten as:

$$\dot{S}_6 = c_6 z_7 + K_6 e_6(\lambda_6)(\int_0^t e_6 dt)^{\lambda_6 - 1} - \frac{x_6}{C_f L_f} - \frac{R_f x_8}{C_f L_f} + \\ \frac{x_{14}x_9}{C_f} + \frac{U_d x_5}{C_f L_f} - M_1 + M_2 + M_3 - M_4 - M_5 - \ddot{x}_6^*. \tag{71}$$

For Lyapunov stability and fast transient convergence, $\dot{S}_6$ must behave as follows:

$$\dot{S}_6 = -\rho_6 sgn(S_6). \tag{72}$$

In next step, using (71) and (72) the control law is developed:

$$U_d = \frac{C_f L_f}{x_5}\left[-c_6 z_7 - \rho_6 sgn(S_6) - \frac{x_{14}x_9}{C_f}\right]+ \\ \frac{C_f L_f}{x_5}\left[\frac{x_6}{C_f L_f} - K_6 e_6(\lambda_6)(\int_0^t e_6 dt)^{\lambda_6 - 1}\right] \\ \frac{C_f L_f}{x_5}\left[\frac{R_f x_8}{C_f L_f} + M_1 - M_2 - M_3 + M_4 + M_5 + \ddot{x}_6^*\right]. \tag{73}$$

Similarly, same steps are followed to enforce x_7 to track x_7^* and following tracking errors are defined:

$$e_7 = \dot{x}_7 - \dot{x}_7^*. \tag{74}$$

$$z_8 = \dot{e}_7. \tag{75}$$

Putting the value of $\dot{x}_7$ from (33) in (74) gives:

$$\dot{e}_7 = -\frac{x_7}{RC_f} - x_{14}x_6 + \frac{x_9}{C_f} - \frac{x_{11}}{C_f} - \frac{x_{13}}{C_f} - \dot{x}_7^*. \tag{76}$$

The derivative of the error term z_8 can be expressed using (32), (33), (35), (37), (39), and (40) as:

$$\dot{z}_8 = -\frac{x_7}{C_f L_f} - \frac{R_f x_9}{C_f L_f} - \frac{x_{14}x_8}{C_f} + \frac{U_q x_5}{C_f L_f} \\ - N_1 - N_2 - N_3 - N_4 - N_5 - \ddot{x}_7^*, \tag{77}$$

where, N_1, N_2, N_3, N_4 and N_5 are taken for the simplification and can be presented as:

$$N_1 = \frac{1}{RC_f}\left[-\frac{x_7}{RC_f} - x_{14}x_6 + \frac{x_9}{C_f} - \frac{x_{11}}{C_f} - \frac{x_{13}}{C_f}\right],$$
$$N_2 = x_6 \dot{x}_{14},$$
$$N_3 = x_{14}\left[-\frac{x_6}{RC_f} + x_{14}x_7 + \frac{x_8}{C_f} - \frac{x_{10}}{C_f} - \frac{x_{12}}{C_f}\right],$$
$$N_4 = \frac{1}{C_f}\left[\frac{x_6}{L_l} - \frac{R_l x_{10}}{L_l} + x_{14}x_{11}\right],$$
$$N_5 = \frac{1}{C_f}\left[\frac{x_7}{L_g} - \frac{R_g x_{13}}{L_g} - x_{14}x_{12} - \frac{W_2}{L_g}\right]. \tag{78}$$

The fast integral terminal sliding mode surface and its derivative can be calculated as:

$$S_7 = z_8 + c_7 e_7 + K_7\left(\int_0^t e_7 dt\right)^{\lambda_7}, \tag{79}$$

$$\dot{S}_7 = \dot{z}_8 + c_7 \dot{e}_7 + K_7 e_7(\lambda_7)\left(\int_0^t e_7 dt\right)^{\lambda_7 - 1}, \tag{80}$$

where $c_7 > 0$ and $K_7 > 0$ are the design parameters, and λ_7 is the positive number. By substituting the values of $\dot{e}_7$ and $\dot{z}_8$ in (80), the equation can be expressed as:

$$\dot{S}_7 = c_7 z_8 + K_7 e_7(\lambda_7)(\int_0^t e_7 dt)^{\lambda_7 - 1} - \frac{x_7}{C_f L_f} - \frac{R_f x_9}{C_f L_f} \\ - \frac{x_{14}x_8}{C_f} + \frac{U_q x_5}{C_f L_f} - N_1 - N_2 - N_3 - N_4 - N_5 - \ddot{x}_7^*. \tag{81}$$

To guarantee the stable operation of VSI, $\dot{S}_7$ should act as:

$$\dot{S}_7 = -\rho_7 sgn(S_7). \tag{82}$$

The following control law is obtained using (81) and (82):

$$U_q = \frac{C_f L_f}{x_5}[-c_7 z_8 - \rho_7 sgn(S_7) - K_7 e_7(\lambda_7)(\int_0^t e_7 dt)^{\lambda_7 - 1}]+ \\ \frac{C_f L_f}{x_5}\left[\frac{x_7}{C_f L_f} + \frac{R_f x_9}{C_f L_f} + \frac{x_{14}x_8}{C_f}\right]+ \\ \frac{C_f L_f}{x_5}[N_1 + N_2 + N_3 + N_4 + N_5 + \ddot{x}_7^*]. \tag{83}$$

The control laws expressed in (73) and (83) are used to generate the duty cycle for the VSI during islanding mode with the goal to regulate the voltages for the AC loads. During grid-connected mode, the microgrid operates at current control manner. Phase-locked loop (PLL) is used to find the grid voltages and frequency. The VSI will function to provide the frequency support to the utility grid. Generally, during the grid-connected mode, VSI is used to stabilize the DC bus for DC loads and to exchange power between micro and utility grid. However, in the considered scenario, the DC bus voltage is maintained by HESS. While VSI operates in current control mode to provide frequency support to the utility grid. x_8^*, and x_9^* are the reference trajectories for the dynamics x_8, and x_9. The reference trajectory x_8^* represents the current injected from micro to utility grid to achieve the desired frequency, and can be calculated using the following equation:

$$x_8^* = \frac{1}{x_6}\left[\frac{2}{3}(P_m + K_{14}(x_{14} - x_{14}^*)) - x_7 x_9\right], \tag{84}$$
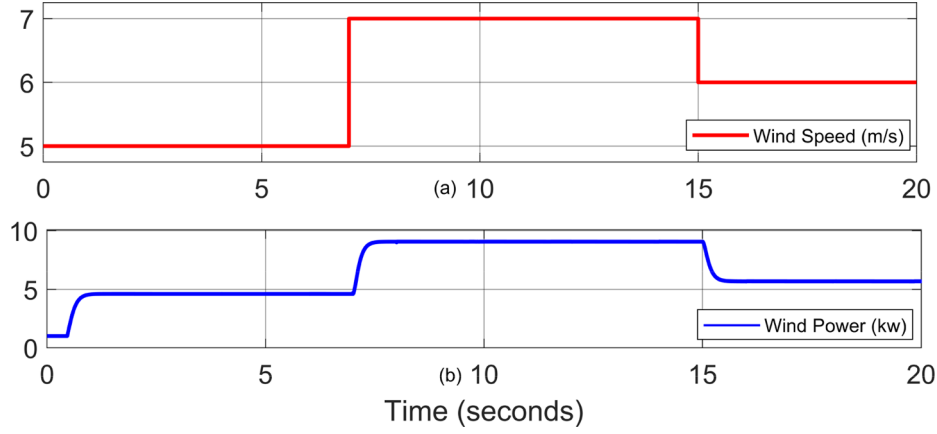
Fig. 7. (a) Wind speed. (b) Wind power (MPPT).

where K_{14} is the gain parameter, and x_{14}^* is the desired frequency. The (84) is computed by solving the (40) for x_8. Defining the integral terminal sliding mode surfaces for the tracking errors e_8, and e_9:

$$S_8 = e_8 + K_8 \left(\int_0^t e_8 dt \right)^{\lambda_8}, \tag{85}$$

$$S_9 = e_9 + K_9 \left(\int_0^t e_9 dt \right)^{\lambda_9}. \tag{86}$$

Taking the derivative of sliding surfaces give:

$$\dot{S}_8 = \dot{e}_8 + K_8 e_8 (\lambda_8) \left(\int_0^t e_8 dt \right)^{\lambda_8 - 1}, \tag{87}$$

$$\dot{S}_9 = \dot{e}_9 + K_9 e_9 (\lambda_9) \left(\int_0^t e_9 dt \right)^{\lambda_9 - 1}. \tag{88}$$

Substituting the value of $\dot{e}_8$ and $\dot{e}_9$ in (87) and (88) gives:

$$\dot{S}_8 = -\frac{x_6}{L_f} - \frac{R_f x_8}{L_f} + x_{14} x_9 + \frac{U_d x_5}{L_f} - x_8^* + K_8 e_8 (\lambda_8) \left(\int_0^t e_8 dt \right)^{\lambda_8 - 1}, \tag{89}$$

$$\dot{S}_9 = -\frac{x_7}{L_f} - \frac{R_f x_9}{L_f} - x_{14} x_8 + \frac{U_q x_5}{L_f} - x_9^* + K_9 e_9 (\lambda_9) \left(\int_0^t e_9 dt \right)^{\lambda_9 - 1}. \tag{90}$$

To stabilize the dynamics of VSI, control laws must be selected for $\dot{S}_8$ and $\dot{S}_9$ to behave as follows:

$$\dot{S}_8 = -\rho_8 sgn(S_8), \tag{91}$$

$$\dot{S}_9 = -\rho_9 sgn(S_9). \tag{92}$$

By comparing (89), and (91), control law U_d can be obtained as follows:

$$U_d = \frac{L_f}{x_5} \left[\frac{x_6}{L_f} + \frac{R_f x_8}{L_f} - x_{14} x_9 - \rho_8 sgn(S_8) \right] + \frac{L_f}{x_5} [x_8^* - K_8 e_8 (\lambda_8) (\int_0^t e_8 dt)^{\lambda_8 - 1}]. \tag{93}$$

Similarly, by comparing (90), and (92), control law U_q can be obtained as follows:

$$U_q = \frac{L_f}{x_5} \left[\frac{x_7}{L_f} + \frac{R_f x_9}{L_f} + x_{14} x_8 - \rho_9 sgn(S_9) \right] + \frac{L_f}{x_5} [x_9^* - K_9 e_9 (\lambda_9) (\int_0^t e_9 dt)^{\lambda_9 - 1}]. \tag{94}$$

The control laws expressed in (93) and (94) are used to generate the duty cycle for the VSI during grid-connected mode and guarantee the convergence of error trajectories, e_8 and e_9. The goal of these generated control signals is to ensure frequency support to the utility grid by regulating both active and reactive power. In the next step, a

positive definite Lyapunov candidate V is introduced for the stability analysis and can be taken as:

$$V = \frac{1}{2}s_1^2 + \frac{1}{2}s_2^2 + \frac{1}{2}s_3^2 + \frac{1}{2}s_4^2 + \frac{1}{2}s_5^2 + \frac{1}{2}s_6^2 + \frac{1}{2}s_7^2 + \frac{1}{2}s_8^2 + \frac{1}{2}s_9^2. \tag{95}$$

To ensure the asymptotic convergence, the time derivative of V must be negative semi-definite and can be presented as:

$$\dot{V} = s_1 \dot{s}_1 + s_2 \dot{s}_2 + s_3 \dot{s}_3 + s_4 \dot{s}_4 + s_5 \dot{s}_5 + s_6 \dot{s}_6 + s_7 \dot{s}_7 + s_8 \dot{s}_8 + s_9 \dot{s}_9. \tag{96}$$

Putting the values of $\dot{s}_1, \dot{s}_2, \dot{s}_3, \dot{s}_4, \dot{s}_5, \dot{s}_6, \dot{s}_7, \dot{s}_8, \dot{s}_9$ gives:

$$\dot{V} = -\rho_1 |s_1| - \rho_2 |s_2| - \rho_3 |s_3| - \rho_4 |s_4| - \rho_5 |s_5| - \rho_6 |s_6| - \rho_7 |s_7| - \rho_8 |s_8| - \rho_9 |s_9|. \tag{97}$$

Hence, the designed controller's asymptotic stability is ensured by using the Lyapunov stability criteria.

4. Results and discussion

The simulations of the AC/DC hybrid microgrid are carried out on MATLAB/Simulink. The parameters and configuration of the microgrid used for the simulations are listed in Table 1–3. The aim of the simulation is to ensure the stable operation of the hybrid AC/DC microgrid by keeping the DC and AC bus voltages constant. The CPLs on the DC side are varied between 15 kW to 25 kW, and linear loads on the AC are switched between 50 Ω and 30 Ω. Two cases based on islanding mode and grid-connected mode were investigated to analyze the performance of the proposed centralized integral terminal sliding mode control (ITSMC) and results are compared against the sliding mode control (SMC) and Lyapunov redesign (CLF). The simulation time for the system is $t = 20$ s. The reference for the controller is provided by high-level controller which is not considered in this study but it is assumed that it will always ensure the energy balance. The change in wind speed and the output power produced by the wind energy system are illustrated in Fig. 7a and b, respectively. It can be observed that when the wind speed jumps from 5 m/s to 7 m/s at $t = 7$ s, the output power of the wind turbine increases as well. Similarly, when the wind speed falls from 7 m/s to 6 m/s at $t = 15$ s, the output power decreases.

4.1. Islanding mode (Case 1)

In Case 1, the dynamic and steady state performance of the microgrid is analyzed when it is operating in islanding mode. Fig. 8 demonstrates the power output of FC, the charging and discharging power of the battery and UC, and the DC load power. It can be observed that the battery and UC follow the reference signal generated by the high-level controller after every 2 s to keep the power balance. During $t = 0 - 5$, due to low wind speed, the output power generated by wind is low. Hence, battery and UC both discharge to provide power along with FC. At 5 s, the load jumps from 15 kW to 20 kW. During
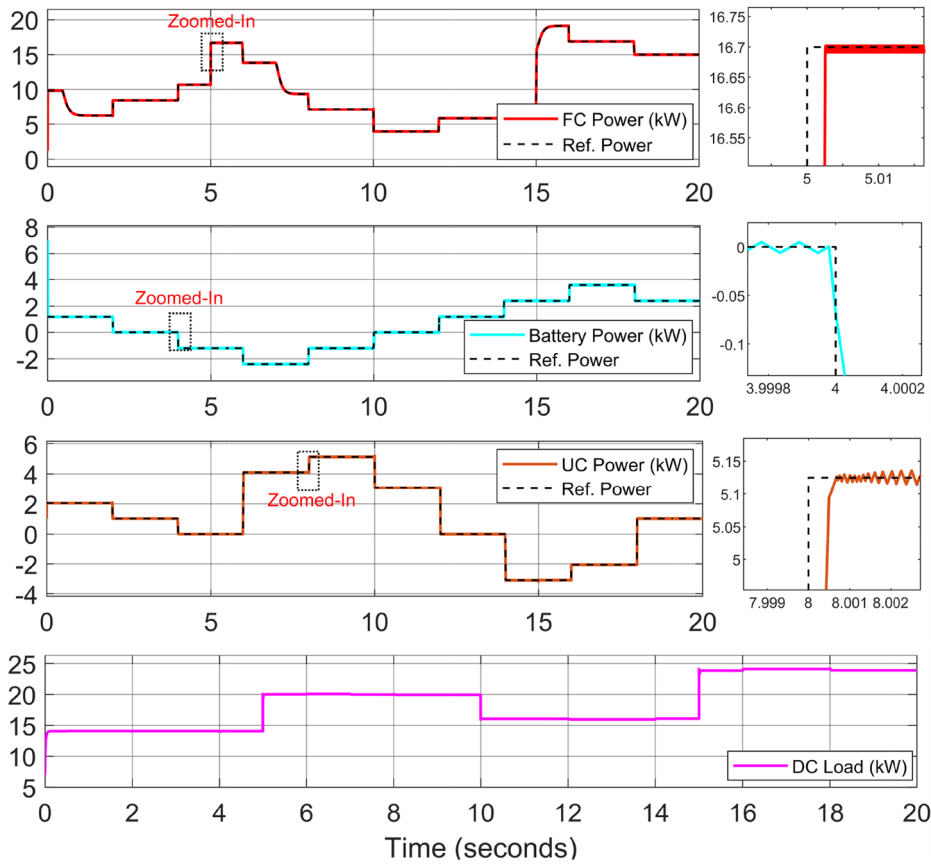
Fig. 8. DC side powers during islanding mode.

$t = 5 - 7$ s, the FC output power is increased to support the load. At 7 s, as the wind power increases from 5 kW to 9 kW, the burden on FC decreases and UC starts to charge, while battery keeps supplying power along with FC. Another important milestone can be observed at 14 s, as the battery starts to charge and FC and UC along with wind energy support the load. At 15, load jumps from 16 kW to 24 kW while the wind power decreases. During 15–20 s, FC and UC both supply power to support the load. It must be noted that during all the stages, FC is

operated within its rated limits to avoid the over and under-utilization of hydrogen for normal operation.

Fig. 9 shows the DC bus voltage regulation. The performance of the proposed ITSMC is compared with SMC and CLF. It can be observed that the voltage strictly tracks the reference value of 400 V for the whole considered period; the proposed ITSMC achieves the steady state in just $t = 0.07$ s, where large overshoot, and settling time can be observed in case of SMC and CLF. At 5 s, transients can be observed
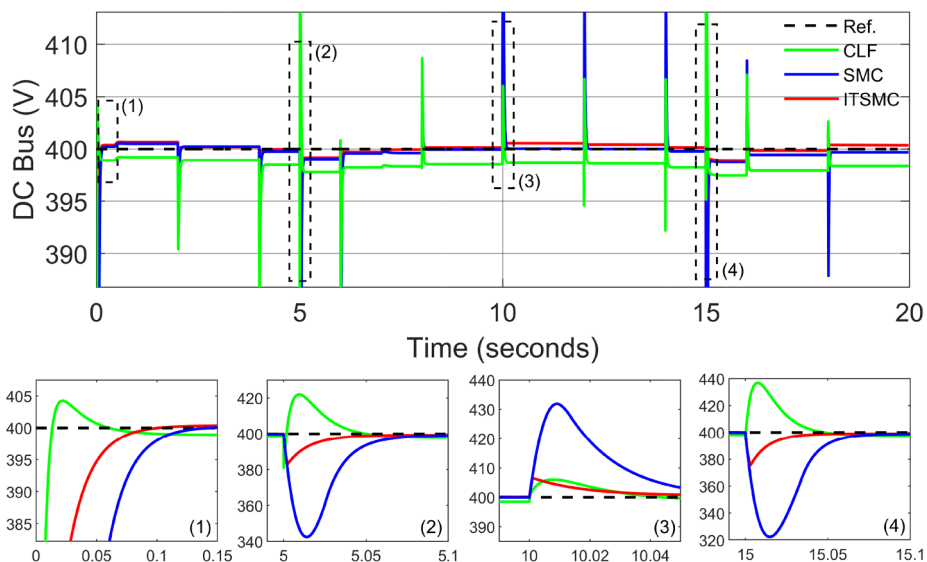

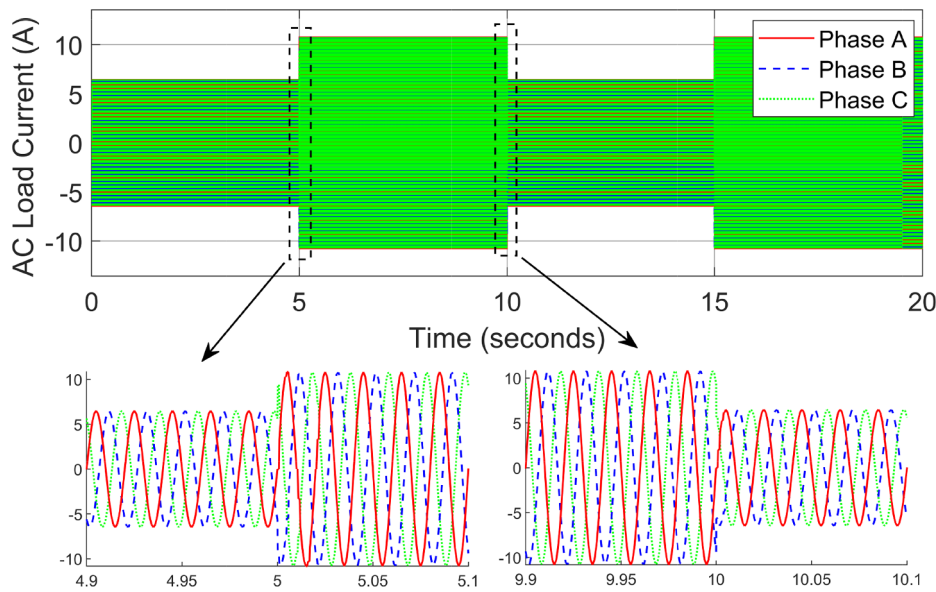**Fig. 9.** DC bus voltage dynamics during islanding mode.

Fig. 10. AC load current during islanding mode.

because of the abrupt change in DC and AC load but ITSMC shows better dynamic performance as compared to the other controllers. At 10 s SMC exhibit larger overshoot and settling time as compared to the ITSMC and CLF. Similarly, at 15 s, ITSMC shows superior performance and fast response to transients.

Figs. 10 and 11, shows the performance of the AC subgrid. In islanding mode, the main objective of the controller is to keep the AC voltage and frequency stable at the AC subgrid. With this goal in mind, the control law for the VSI is developed. From the zoomed-in waveform plotted in Fig. 11, the stable AC bus voltage, and frequency can be observed while the AC load varied between 6A and 10A. The AC load waveform is shown in Fig. 10 with zoomed-in plots at 5 s and 10 s. The smooth sinusoidal current waveforms are observed.

4.2. Grid-connected mode (Case 2)

In Case 2, the performance of the microgrid is evaluated in the gird-connected mode. A special framework is studied based on microgrid's response to the frequency regulation request from the utility grid. Fig. 12 shows the waveforms of the power injected by the FC, the charging and discharging power of the battery and UC, and the power consumed by the load. It can be observed that the battery and UC follow the reference signal generated by the high-level controller after every 2 s to keep the power balance. During $t = 0 - 7$ s, the load is set to 15 kW. Wind energy and FC supply most of the power while the additional support is provided by the UC. The battery charges during this

period. During $t = 7 - 15$ s, the load jumps from 15 kW to 25 kW as the flow of current from micro to utility grid increases. It can be observed that during this time period, the FC output power increases to support the load. Meanwhile, the additional energy is provided by UC and battery. During $t = 15 - 20$ s, the load decreases from 25 kW to 18 kW. Both FC and battery support the load but a decrease in FC output power can be noticed. Furthermore, UC starts to charge as well.

Fig. 13 shows the DC bus voltage regulation during the grid-connected mode. The comparative analysis of the proposed ITSMC technique is done with SMC and CLF. The strict tracking of the DC bus voltage to the reference value of 400 V can be observed for the whole considered period. It can be noticed that the proposed ITSMC achieves the steady state evidently faster than SMC and CLF in just $t = 0.1$ s. At 7 s, transients can be seen as the load changes because of the increase in the flow of current from micro to the utility grid, but ITSMC shows better dynamic performance as compared to the other controllers. The zoomed-in waveform at 9 s depicts the better steady state performance of the ITSMC with very little steady state error as compared to the CLF and SMC. Another spike in performance can be noticed at 15, when the load changes again. Both ITSMC and SMC show a similar performance where in the case of CLF, overshoot can be observed.

Figs. 14 and 15, shows the performance of the AC side during gird-connected mode. During grid-connected mode, the prime task of the controller is to provide the frequency support to the utility grid. With this goal in mind, the control law for the VSI is developed. The frequency variation is induced in the AC side by altering the equilibrium
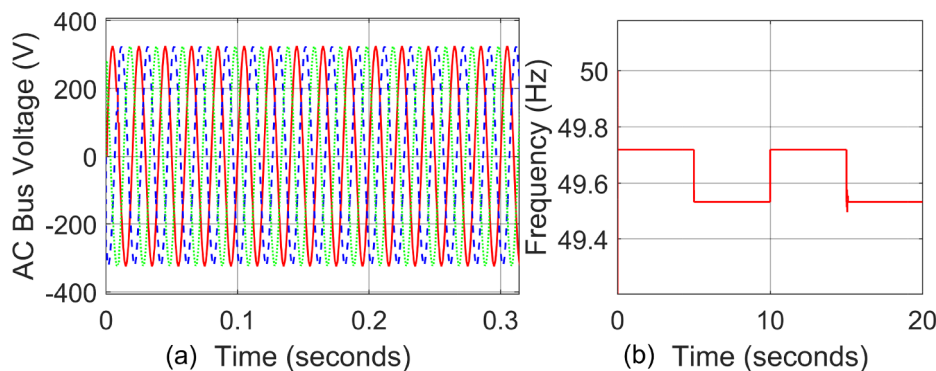

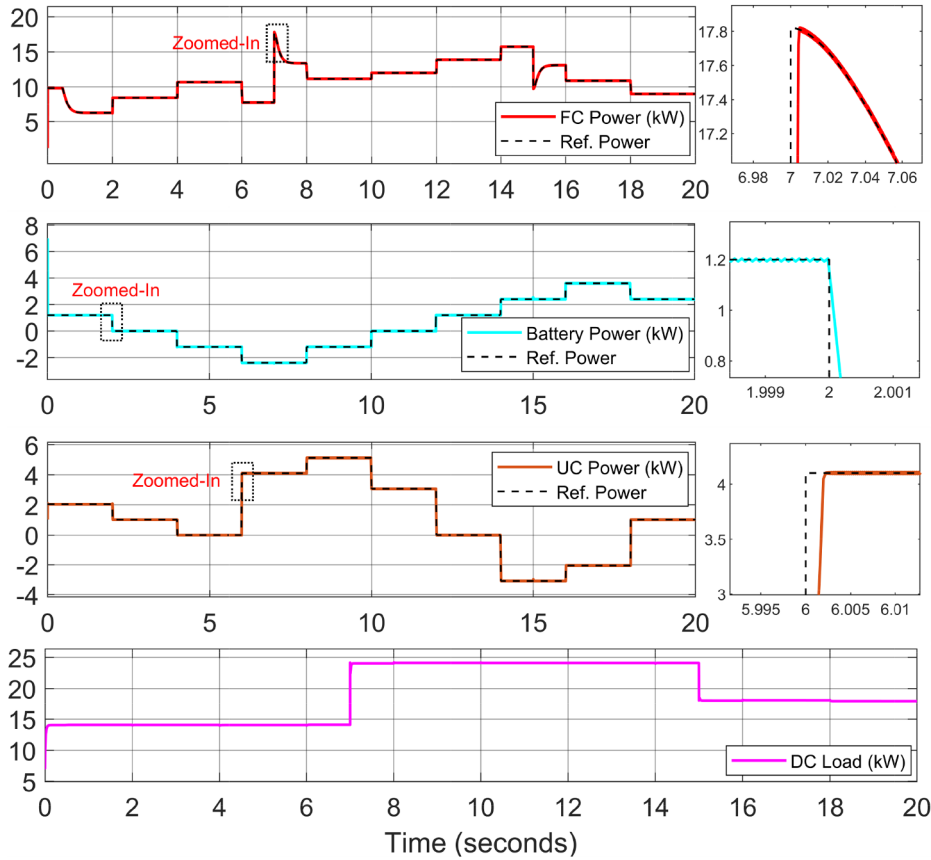**Fig. 11.** (a) AC bus voltage. (b) Frequency.

Fig. 12. DC side powers during grid-connected mode.

between the electric torque and mechanical torque. From the zoomed-in waveform plotted in Fig. 14, the effective controller performance can be noticed to stabilize the frequency of the utility grid by injecting current to keep the balance between generation and demand. Fluctuations can be observed at 0 s, 7 s and 15 s but the proposed ITSMC controller shows a fast dynamic response. The current flow from micro to the utility grid is shown in Fig. 15 with zoomed-in plots at 7 s and 15 s. The smooth sinusoidal current waveforms are observed.

4.3. Hardware in the loop analysis

The performance of the proposed ITSMC is further evaluated by conducting real-time controller hardware in the loop (C-HIL) experiments, as shown in Fig. 16. C-HIL simulations are a cost-effective way to check the performance of the controllers prior to the practical implementation. In these C-HIL experiments, the controllers are implemented using C2000 Delfino MCU F28379D LaunchPad to generate
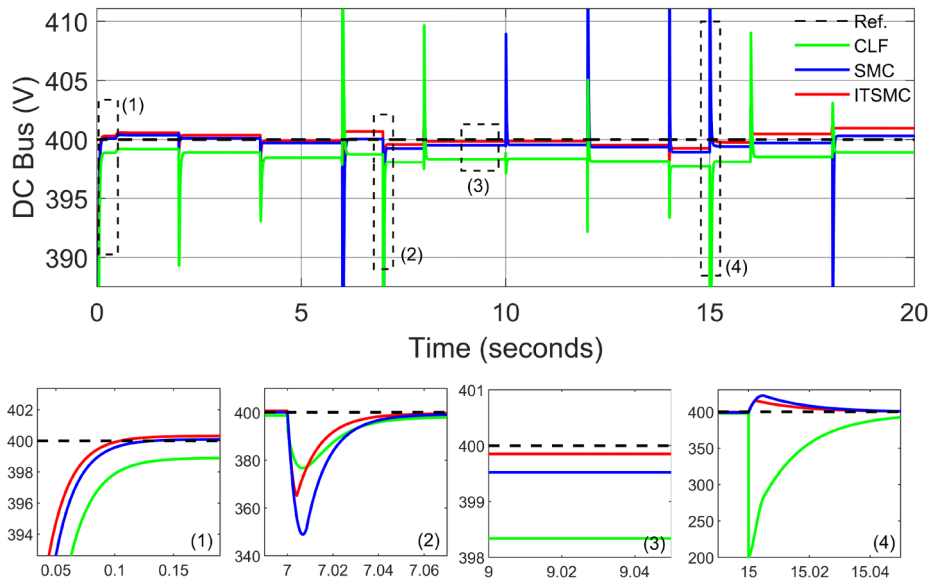

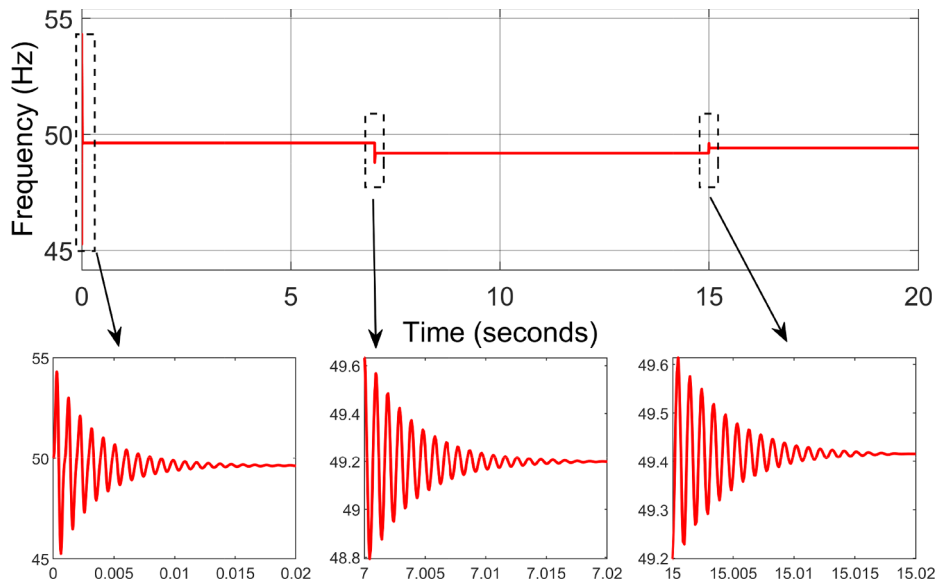**Fig. 13.** DC bus voltage dynamics during grid-connected mode.
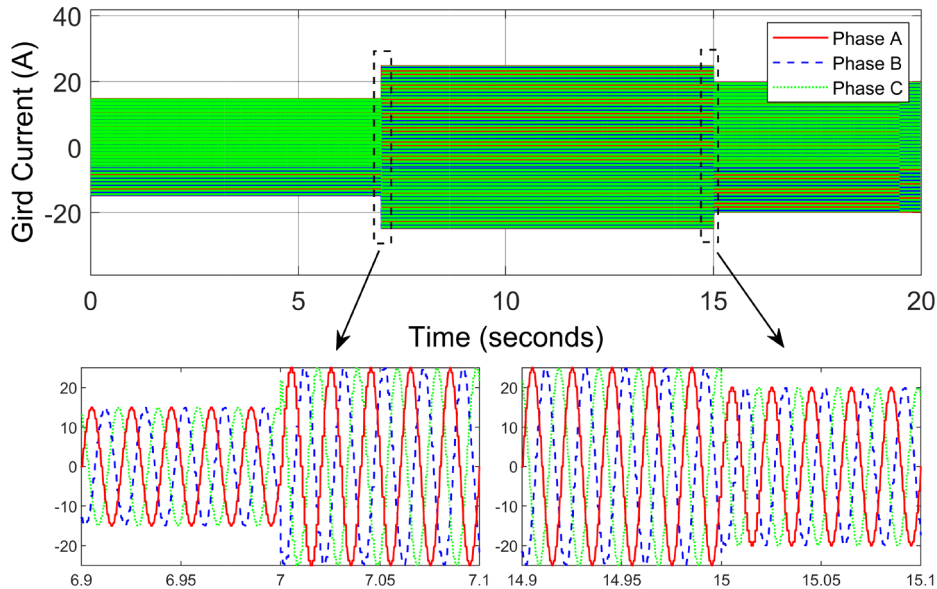
Fig. 14. Frequency variation in the AC side.

Fig. 15. Current flow from micro to the utility grid.
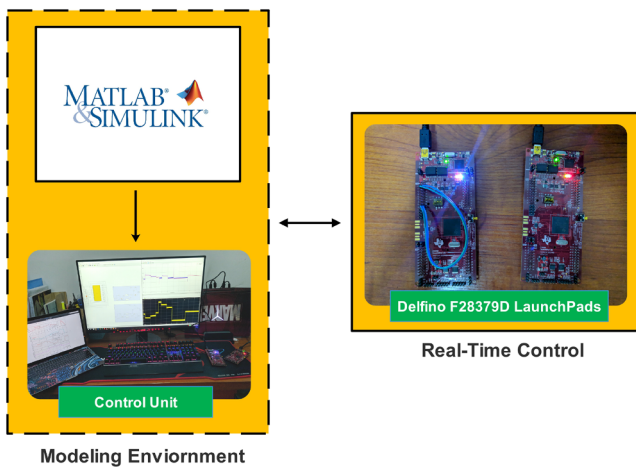
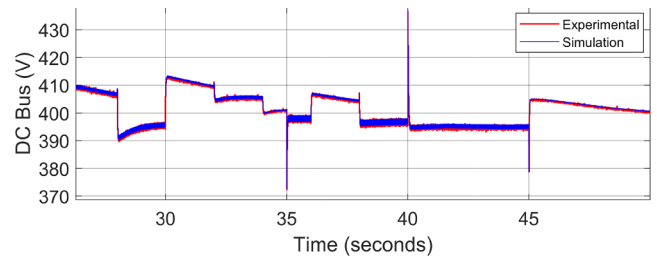

Fig. 16. C-HIL setup.

Fig. 17. DC bus voltage during islanding mode.

the control signals, while the hybrid AC/DC microgrid environment is modeled on MATLAB/Simulink. To facilitate the C-HIL experiments, the wind energy system is operated to supply the constant output power of 12 kW. The C-HIL tests are performed under islanding and grid-connected mode, and the results are compared with simulation results for the verification.
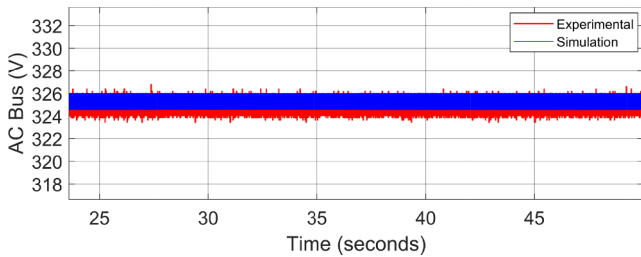
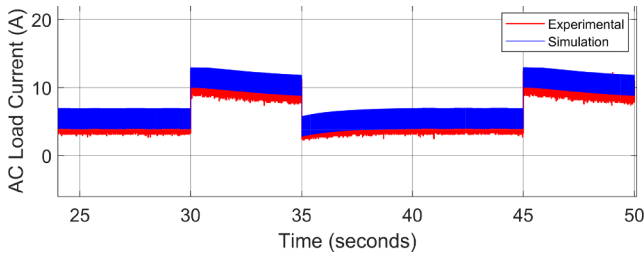**Fig. 18.** AC bus voltage (V_d) in $dq - frame$ during islanding mode.

Fig. 19. AC load current (I_{ld}) in $dq - frame$ during islanding mode.

Fig. 20. DC bus voltage during grid-connected mode.

Fig. 21. Current flow from micro to utility grid (I_{gd}) in $dq - frame$ during grid-connected mode.
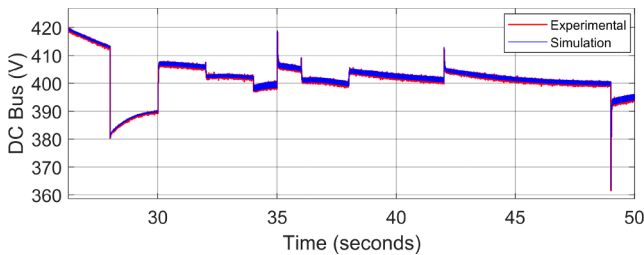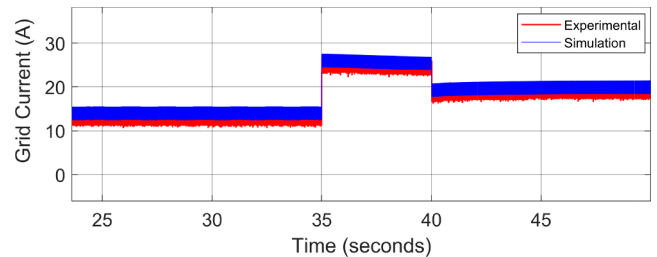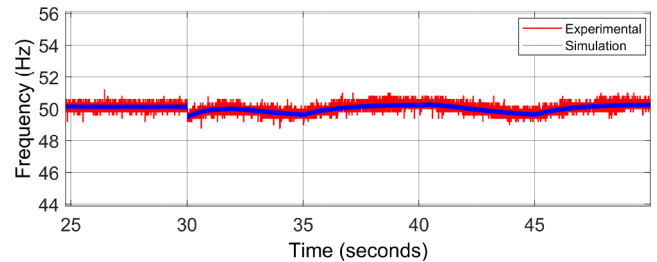

Fig. 22. Frequency variation in the AC side during grid-connected mode.

4.3.1. Islanding mode

Figs. 17 and 18 shows the DC and AC bus voltage regulation during islanding mode. Although, few spikes can be noticed in Fig. 17 as the load changes, but they are well within the rated value. Fig. 19, shows the response of the AC load current in the dq-frame. The experimental results are compared with simulation results and satisfactory performance is observed.

4.3.2. Grid-connected mode

Fig. 20 shows the regulation of DC bus voltage under grid-connected mode. Spikes can be observed at $t = 35$ s and $t = 40$ s, because of the variation in grid current. However, the controller shows a fast dynamic response to ensure the stable DC bus voltage. Fig. 21 shows the flow of current from micro to the utility grid in dq-frame. From Fig. 22 it can be observed that frequency tracks its reference value of 50 Hz. The experimental results validate the simulation results and show the good performance of the controller.

5. Conclusion

This paper provides the ITSMC based nonlinear control approach for the hybrid AC/DC microgrid operating in islanding and grid-connected mode. The performance of the proposed ITSMC controller under different cases is evaluated by simulating it on MATLAB/Simulink, and the results show how the proposed controller provides superior performance to SMC and CLF. The main target of keeping DC and AC subgrid stable during islanding and grid-connected mode is successfully achieved. It is worth mentioning that in grid-connected mode, microgrid's response to the frequency regulation request from the utility grid is studied and satisfactory performance is observed. Furthermore, stability analysis is performed using Lyapunov candidate to ensure the asymptotic stability of the hybrid AC/DC microgrid. Finally, real-time C-HIL based tests have been executed to further validate the performance of the proposed framework. Experimental results indicate that the proposed controller achieves the stable DC bus voltage in spite of variable power output from the renewable sources and on/off grid scenarios. Future work involves constructing the real microgrid in the laboratory to analyze the performance of the proposed method by conducting experimental tests.

Declaration of Competing Interest

The authors declare that they have no known competing financial interests or personal relationships that could have appeared to influence the work reported in this paper.

Appendix A

See Tables 1–3.

Table 1
Parameters of wind energy system.

Wind Turbine Model	
Air density	1.225 kg/m^3
Rated Wind Speed	5 m/s
Rotor Diameter	5.5 m
λ_{opt}	7.5
C_{p-max}	0.43

PMSG	
Stator phase resistance	0.425 Ω
Armature inductance	0.000395H
Flux Linkage	0.433 Wb
Moment of Inertia	0.011 kg·m^2
Viscous Damping	0.001889 N·m·s

Table 2
Parameters of energy storage system.

Fuel Cell	
Voltage	346 V
Rated Power	20 KW

Lead Acid Battery	
Voltage	540 V
Rated Capacity	33.9 Ah
Maximum Charge Current	17.5 A
Maximum Discharge Current	30 A

UC Bank	
Voltage	205 V
Rated Capacity	2700 F

Table 3
Parameters of simulated AC/DC microgrid.

Configuration	
DC Grid Nominal Voltage	400 V
AC Grid Nominal Voltage	230 V
Frequency	50 Hz
DC bus capacitor	$C_{dc} = 16\ \mu F$
AC bus LC filter	$L_f = 1.5$ mH, $C_f = 45\ \mu F$
DC Loads	Constant Power Loads
AC Loads	Load 1 = 50 Ω, Load 2 = 30 Ω (Linear Loads)

DC-DC Converters	
Inductances L_w, L_{fc}, L_{bat}, L_{uc}	20 mH,20 mH, 3.3 mH, 3.3 mH
Capacitance C_{dc}	16 μF
Switching Frequency	100 kHz

DC-AC Inverter	
Inductances L_l, L_g	1.5 mH, 0.5 mH
Resistances R_f, R_l, R_g	0.15 Ω, 4.5 Ω, 0.1 Ω

Control System	
Gains of Controllers	$\rho_1 = 10000, \rho_2 = 10000$ $\rho_3 = 20000, \rho_4 = 20000$ $\rho_5 = 10000, \rho_6 = 1000, \rho_7 = 20000$ $\rho_8 = 1000, \rho_9 = 1000$
Gains of Sliding Surfaces	$K_1 = 0.1, K_2 = 0.1, K_3 = 0.3, K_4 = 0.3$ $K_5 = 0.3, K_6 = 0.1, K_7 = 0.3, K_8 = 0.1, K_9 = 0.2$ $\lambda_1 = 1.5, \lambda_2 = 1.5, \lambda_3 = 1.5, \lambda_4 = 1.5$ $\lambda_5 = 1.5, \lambda_6 = 1.5, \lambda_7 = 1.5, \lambda_8 = 1.5, \lambda_9 = 1.5$

References

[1] Khare V, Nema S, Baredar P. Solar–wind hybrid renewable energy system: a review. Renew Sustain Energy Rev 2016;58:23–33.

[2] Zhou X, Zhou L, Chen Y, Guerrero JM, Luo A, Wu W, et al. A microgrid cluster structure and its autonomous coordination control strategy. Int J Electr Power Energy Syst 2018;100:69–80.

[3] Wang P, Goel L, Liu X, Choo FH. Harmonizing ac and dc: a hybrid ac/dc future grid solution. IEEE Power Energ Mag 2013;11(3):76–83.

[4] Yang P, Xia Y, Yu M, Wei W, Peng Y. A decentralized coordination control method for parallel bidirectional power converters in a hybrid ac–dc microgrid. IEEE Trans Industr Electron 2017;65(8):6217–28.

[5] Sorknæs P, Djørup SR, Lund H, Thellufsen JZ. Quantifying the influence of wind power and photovoltaic on future electricity market prices. Energy Convers Manage 2019;180:312–24.

[6] Sharma RK, Mishra S. Dynamic power management and control of a pv pem fuel-cell-based standalone ac/dc microgrid using hybrid energy storage. IEEE Trans Ind Appl 2017;54(1):526–38.

[7] El-Sharkh M, Rahman A, Alam M, Byrne P, Sakla A, Thomas T. A dynamic model for a stand-alone pem fuel cell power plant for residential applications. J Power Sources 2004;138(1–2):199–204.

[8] Khan M, Iqbal M. Dynamic modeling and simulation of a small wind–fuel cell hybrid energy system. Renew Energy 2005;30(3):421–39.

[9] Tummuru NR, Mishra MK, Srinivas S. Dynamic energy management of renewable grid integrated hybrid energy storage system. IEEE Trans Industr Electron 2015;62(12):7728–37.

[10] Tani A, Camara MB, Dakyo B. Energy management in the decentralized generation systems based on renewable energy—ultracapacitors and battery to compensate the wind/load power fluctuations. IEEE Trans Ind Appl 2015;51(2):1817–27.

[11] Dougal RA, Liu S, White RE. Power and life extension of battery-ultracapacitor hybrids. IEEE Trans Compon Packag Technol 2002;25(1):120–31.

[12] Ma T, Cintuglu MH, Mohammed OA. Control of a hybrid ac/dc microgrid involving energy storage and pulsed loads. IEEE Trans Ind Appl 2016;53(1):567–75.

[13] Babazadeh M, Karimi H. A robust two-degree-of-freedom control strategy for an islanded microgrid. IEEE Trans Power Deliv 2013;28(3):1339–47.

[14] Kumar M, Srivastava S, Singh S. Control strategies of a dc microgrid for grid connected and islanded operations. IEEE Trans Smart Grid 2015;6(4):1588–601.

[15] Kakigano H, Miura Y, Ise T. Distribution voltage control for dc microgrids using fuzzy control and gain-scheduling technique. IEEE Trans Power Electron 2013;28(5):2246–58.

[16] Mohamed YA-RI, Zeineldin HH, Salama M, Seethapathy R. Seamless formation and robust control of distributed generation microgrids via direct voltage control and optimized dynamic power sharing. IEEE Trans Power Electron 2012;27(3):1283–94.

[17] Singh S, Fulwani D, Kumar V. Robust sliding-mode control of dc/dc boost converter feeding a constant power load. IET Power Electron 2015;8(7):1230–7.

[18] Armghan H, Yang M, Wang M, Ali N, Armghan A. Nonlinear integral backstepping based control of a dc microgrid with renewable generation and energy storage systems. Int J Electr Power Energy Syst 2020;117:105613.

[19] Liang B, Kang L, He J, Zheng F, Xia Y, Zhang Z, et al. Coordination control of hybrid ac/dc microgrid. J Eng 2019;2019(16):3264–9.

[20] Liu X, Wang P, Loh PC. A hybrid ac/dc microgrid and its coordination control. IEEE Trans Smart Grid 2011;2(2):278–86.

[21] Loh PC, Li D, Chai YK, Blaabjerg F. Autonomous operation of hybrid microgrid with ac and dc subgrids. IEEE Trans Power Electron 2012;28(5):2214–23.

[22] Wang P, Jin C, Zhu D, Tang Y, Loh PC, Choo FH. Distributed control for autonomous operation of a three-port ac/dc/ds hybrid microgrid. IEEE Trans Industr Electron 2014;62(2):1279–90.

[23] Thounthong P, Luksanasakul A, Koseeyaporn P, Davat B. Intelligent model-based control of a standalone photovoltaic/fuel cell power plant with supercapacitor energy storage. IEEE Trans Sustain Energy 2012;4(1):240–9.

[24] Xia Y, Peng Y, Yang P, Yu M, Wei W. Distributed coordination control for multiple bidirectional power converters in a hybrid ac/dc microgrid. IEEE Trans Power Electron 2016;32(6):4949–59.

[25] Jin C, Loh PC, Wang P, Mi Y, Blaabjerg F. Autonomous operation of hybrid ac-dc microgrids. 2010 IEEE international conference on sustainable energy technologies (ICSET). IEEE; 2010. p. 1–7.

[26] Guangqian D, Feng G, Zhang S, Loh PC, Blaabjerg F. Control of hybrid ac/dc microgrid under islanding operational conditions. J Modern Power Syst Clean Energy 2014;2(3):223–32.

[27] Guerrero JM, Loh PC, Lee T-L, Chandorkar M. Advanced control architectures for intelligent microgrids—part ii: power quality, energy storage, and ac/dc microgrids. IEEE Trans Industr Electron 2012;60(4):1263–70.

[28] Hu J, Shan Y, Xu Y, Guerrero JM. A coordinated control of hybrid ac/dc microgrids with pv-wind-battery under variable generation and load conditions. Int J Electr Power Energy Syst 2019;104:583–92.

[29] Vasquez JC, Guerrero JM, Luna A, Rodríguez P, Teodorescu R. Adaptive droop control applied to voltage-source inverters operating in grid-connected and islanded modes. IEEE Trans Ind Electron 2009;56(10):4088–96.

[30] Wang C, Li X, Guo L, Li YW. A nonlinear-disturbance-observer-based dc-bus voltage control for a hybrid ac/dc microgrid. IEEE Trans Power Electron 2014;29(11):6162–77.

[31] Iovine A, Siad SB, Damm G, De Santis E, Di Benedetto MD. Nonlinear control of an ac-connected dc microgrid. IECON 2016–42nd annual conference of the IEEE industrial electronics society. IEEE; 2016. p. 4193–8.

[32] Roy TK, Mahmud MA. Dynamic stability analysis of hybrid islanded dc microgrids using a nonlinear backstepping approach. IEEE Syst J 2017;12(4):3120–30.

[33] Baghaee HR, Mirsalim M, Gharehpetian GB, Talebi HA. A decentralized power management and sliding mode control strategy for hybrid ac/dc microgrids including renewable energy resources. IEEE Trans Industr Inf 2017.

[34] Housseini B, Okou AF, Beguenane R. Robust nonlinear controller design for on-grid/off-grid wind energy battery-storage system. IEEE Trans Smart Grid 2017;9(6):5588–98.

[35] Dehkordi NM, Sadati N, Hamzeh M. Robust backstepping control of an interlink converter in a hybrid ac/dc microgrid based on feedback linearisation method. Int J Control 2017;90(9):1990–2004.

[36] Iovine A, Carrizosa MJ, Damm G, Alou P. Nonlinear control for dc microgrids enabling efficient renewable power integration and ancillary services for ac grids. IEEE Trans Power Syst 2018.

[37] Rebours YG, Kirschen DS, Trotignon M, Rossignol S. A survey of frequency and voltage control ancillary services—part i: technical features. IEEE Trans Power Syst 2007;22(1):350–7.

[38] Han Y, Ma R, Cui J. Adaptive higher-order sliding mode control for islanding and grid-connected operation of a microgrid. Energies 2018;11(6):1459.

[39] Abdullah MA, Yatim A, Tan CW, Saidur R. A review of maximum power point tracking algorithms for wind energy systems. Renew Sustain Energy Rev 2012;16(5):3220–7.